OPTICA

Extreme ultraviolet high-harmonic interferometry of excitation-induced bandgap dynamics in solids

Lisa-Marie Koll,[1,†] Simon Vendelbo Bylling Jensen,[2,†] Pieter J. van Essen,[3,†] Brian de Keijzer,[3,†] Emilia Olsson,[3] Jon Cottom,[3] Tobias Witting,[1] Anton Husakou,[1] Marc J. J. Vrakking,[1] Lars Bojer Madsen,[2] Peter M. Kraus,[3,4] and Peter Jürgens[1,3,*]

[1]Max-Born-Institute for Nonlinear Optics and Short Pulse Spectroscopy, Max-Born-Str. 2A, 12489 Berlin, Germany
[2]Department of Physics and Astronomy, Aarhus University, Ny Munkegade 120, DK-8000, Denmark
[3]Advanced Research Center for Nanolithography (ARCNL), Science Park 106, 1098 XG Amsterdam, Netherlands
[4]Department of Physics and Astronomy, and LaserLaB, Vrije Universiteit, De Boelelaan 1105, 1081 HV Amsterdam, Netherlands
[†]These authors contributed equally to this work.
*juergens@mbi-berlin.de

Received 28 February 2025; revised 15 September 2025; accepted 21 September 2025; published 3 October 2025

Interferometry is a fundamental technique in physics, enabling precise measurements through the interference of waves. High-harmonic generation (HHG) in solids has emerged as a powerful method for probing ultrafast electronic dynamics within crystalline structures. In this study, we employed extreme ultraviolet (XUV) high-harmonic interferometry with phase-locked XUV pulse pairs to investigate excitation-induced bandgap dynamics in solids. Our experiments on amorphous SiO_2 and crystalline MgO, complemented by analytical modeling and semiconductor Bloch equation simulations, reveal a correlation between phase variations in harmonic emission that are consistent with bandgap modifications. These findings suggest a potential pathway for time-resolved, all-optical probing of band structure dynamics, advancing prospects for petahertz-scale electronic applications and attosecond diagnostics of carrier dynamics.

https://doi.org/10.1364/OPTICA.559022

1. INTRODUCTION

Optical interferometry stands as a cornerstone in the annals of optical sciences, tracing its roots back to seminal works such as the observation of the diffraction pattern in single- and double-slit experiments. In the field of ultrafast physics, interferometry has been widely used for the characterization of ultrashort laser pulses using the technique of Spectral Phase Interferometry for Direct Electric-field Reconstruction (SPIDER) [1]. Further, the transient alteration of the optical properties of transparent solids has been studied by spectral interferometry, yielding information on the dynamic modification of the refractive index during ultrafast light-matter interaction [2,3]. The advent of attosecond science, marked by milestone achievements such as the experimental generation of attosecond pulse trains [4,5] and isolated attosecond pulses [6]—recognized with the Nobel Prize in Physics in 2023 [7–9]—has profoundly impacted the field of ultrafast and nonlinear optics [10]. It has not only facilitated the characterization of attosecond pulses [11] but has also enabled the probing of ultrafast electron wavefunction dynamics [12] and field-induced tunneling ionization [13].

With the pioneering demonstration of high-order harmonic generation (HHG) in solids [14,15], HHG in solids has emerged as a powerful tool for probing ultrafast electronic dynamics [16,17] and band structure properties in condensed matter systems [18–21]. In parallel, the concepts of solid-state HHG and interferometry have first been merged to track the intensity dependence of the dipole phase [22]. For atomic HHG, the dipole phase can be viewed as the phase accumulated by an electron wavepacket during its excursion, semiclassically described by the three-step model [23–25]. Lu *et al.* [22] investigated the spatial interference pattern in the far field, generated by two phase-locked NIR pulses focused on two separate spots in a solid sample. Their results identified intensity-dependent dipole phase variations that were attributed to changes in the nonlinear polarization. In a more recent study, Uchida *et al.* employed a Mach–Zehnder interferometer to track the real-time dynamics of Floquet states in WSe_2 [26].

Our work builds upon these studies by employing spectral interferometry of phase-locked extreme ultraviolet (XUV) pulse pairs to investigate excitation-induced bandgap dynamics in bulk solids. We focus on amorphous SiO_2 and crystalline MgO samples, both of which have been subjects of previous HHG studies [27–31], and were selected to compare materials with markedly different carrier relaxation times and structural order.

In contrast to the earlier experiments performed by Lu *et al.*, we investigate the spectral interference generated by two collinearly propagating phase-locked pulses. Hence, rather than examining

intensity-dependent harmonic phase changes, we investigate excitation-induced phase variations between the two generated XUV pulses. By comparing the interferometric signal at different total intensities while keeping the pulse energies balanced, our approach isolates differential phase shifts induced by photoexcitation of the medium, making it inherently insensitive to static intensity-dependent dipole phase variations.

Unlike coherent modifications of the electronic structure, such as Floquet engineering [32,33] or the dynamical Franz–Keldysh effect [34,35], we observe incoherent modifications resulting from longer-lived carrier excitation, a topic that remains highly debated within the field of strongly excited wide-bandgap solids [36–41]. As a result, our work correlates the observed phase shifts with transient, excitation-induced alterations of the material's bandgap.

Our experimental results are corroborated by numerical calculations based on an analytical model alongside the solution of the semiconductor Bloch equations (SBEs) [42,43]. We observe high-harmonic phase shifts of opposite sign in amorphous SiO_2 and crystalline MgO samples, which we interpret as being consistent with excitation-induced modifications of the electronic structure. As a result, our work introduces a potential technique for all-optical probing of band structure dynamics on femtosecond timescales. These advancements open new opportunities for resolving ultrafast carrier dynamics in solids, enabling direct access to photo-induced band structure changes with subcycle precision.

2. EXPERIMENTAL SETUP

In our experiments, we utilized a few-cycle, near-infrared (NIR) waveform with a central wavelength of 750 nm and a full-width half-maximum intensity pulse duration of approximately 4 fs (measured with a home-built SEA-F-SPIDER [44]). This NIR waveform was divided into two identical copies using a passively and actively stabilized Mach–Zehnder interferometer (MZI), as described in Ref. [45]. At the output of the MZI, the two identical, phase-locked NIR pulses propagated collinearly. The beams were focused onto a bulk solid sample by a single spherical mirror with a focal length of 750 mm. Control over the total pulse energy entering the MZI was achieved using a combination of an achromatic zero-order half-wave plate and a broadband wire-grid polarizer. The temporal separation between the two phase-locked NIR pulses (referred to as $\tau_{NIR-NIR}$) was adjusted by a computer-controlled delay stage within the MZI. Additionally, a second piezo stage was used to actively stabilize the MZI using the interferometric signal of a co-propagating continuous-wave laser as a reference. Depending on the thickness of the solid samples used, we optimized the pulse duration using a pair of fused silica wedges, allowing for precise control of the dispersion. This optimization ensured optimal contrast in the interferogram and well-separated harmonics, facilitating the analysis of the phase for individual harmonics. The wedge position was kept constant throughout all measurements to ensure consistency and reproducibility. The intense NIR pulses interacted with the solid sample, leading to the generation of HHG extending into the XUV spectral range. Due to the phase-locking between the two identical NIR pulses, a phase-locked XUV pulse pair (separated by $\tau_{XUV-XUV} = \tau_{NIR-NIR}$) was produced. The XUV radiation was recollimated and directed toward an XUV spectrometer with the help of a toroidal mirror (TM in Fig. 1). To spectrally resolve the individual harmonics, the beams were reflected by a variable line-spacing grating (labeled VLG in Fig. 1) before being detected by a double-stack microchannel plate (MCP) and a phosphor screen monitored with a CCD camera from outside the vacuum chamber. The VLG could be removed from the beam path with the help of a motorized translation stage to enable the analysis of the NIR beams using a commercial fiber spectrometer (Ocean Optics FLAME-S-VIS-NIR, NIR spectrometer in Fig. 1). XUV and NIR spectra were acquired as a function of the NIR intensity at various NIR–NIR delays. Throughout the measurements, the integrity of the samples was ensured by monitoring the stability of the HHG signal and potential scattering of the fundamental beam from permanent, laser-induced modifications. As demonstrated in prior studies [19], the combination of thin samples and few-cycle laser pulses ensured that the solid samples could withstand extremely high field strengths on the order of several V $Å^{-1}$.

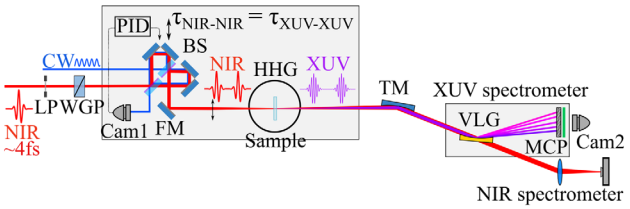

Fig. 1. Experimental setup. A near-infrared (NIR), few-cycle laser pulse was split into two identical copies and focused into a bulk solid sample. The resulting phase-locked extreme ultraviolet (XUV) pulse pair was analyzed with the help of an XUV spectrometer, while the fundamental NIR beam was analyzed with a near-infrared spectrometer. LP, half-wave plate; WGP, wire-grid polarizer; CW, continuous wave stabilization laser; PID, proportional–integral–differential controller; Cam 1, CMOS camera; BS, beam splitters; FM, focusing mirror; TM, toroidal mirror; VLG, variable line-spacing grating; MCP, micro-channel plate + phosphor screen; and Cam2, CCD camera.

3. EXPERIMENTAL RESULTS

In our experiments, we investigated the XUV spectral interferometry signal obtained from amorphous SiO_2 (UV-grade Fused Silica, Corning7980, 10 μm thickness) and crystalline MgO (SurfaceNet, 100 μm thickness, measurements were conducted along the [100] crystallographic direction). For both materials, we observed odd harmonics of orders five to nine, reaching photon energies of approximately ∼16 eV. The maximum detected photon energy was determined by the geometry of the detection unit and does not represent the cutoff of the HHG spectrum [46]. A representative high-harmonic interferogram obtained with an NIR–NIR delay of 30 fs in SiO_2 excited at a peak intensity of 32.3 TW cm^{-2} is shown in Fig. 2(a). A well-defined interference pattern, consisting of periodic minima and maxima, is visible in all detected harmonics (labeled H5, H7, and H9). Despite the substantial bandwidth of the driving NIR pulses, which support durations close to a single optical cycle, we observed well-separated odd harmonics. This separation results from the positive chirp of the NIR pulses, leading to constructive interference of attosecond bursts emitted during each half-cycle [47]. Ideally, the spacing between interference fringes remains constant across the high-harmonic spectrum; however, slight deviations among individual harmonics can be attributed to detector calibration inaccuracies and potential dispersion effects within the solid samples.

Before proceeding with additional analysis of the interferometric measurements, it is essential to ensure the setup's stability.

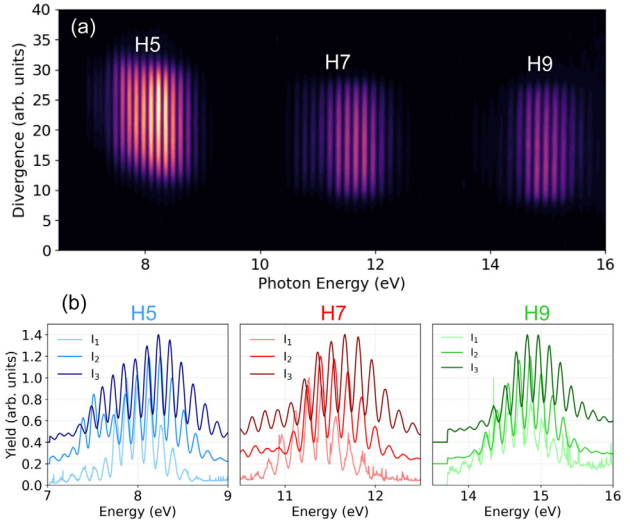

Fig. 2. XUV interferometry in bulk SiO_2. (a) Interferometric pattern of harmonics 5, 7, and 9 at an NIR–NIR delay of 30 fs. (b) Spatially integrated harmonic signal of the individual odd harmonics obtained at different NIR peak intensities ($I_1 = 15.7$ TW cm^{-2}, $I_2 = 32.3$ TW cm^{-2}, and $I_3 = 46.7$ TW cm^{-2}) projected onto the energy axis. The spectra are offset vertically (by 0.2 for I_2 and 0.4 for I_3) for visibility.

A comprehensive characterization and analysis of the stability assessment are provided in Supplement 1 as well as in Ref. [45] demonstrating a stability of below 10 as.

To investigate the field-intensity impact on the interferometric fringe pattern, we modulated the peak intensity of the two phase-locked NIR pulses while maintaining a constant splitting ratio of 50:50 in the MZI. By progressively increasing the intensity of both pulses, we aimed to assess how the interaction of the first NIR pulse, $E_1(\omega, t)$, with the sample influences the subsequent interaction between the second NIR pulse, $E_2(\omega, t-\tau)$, and the sample. This influence manifests as a shift in the minima and maxima observed in the interferometric spectra, reflecting a phase shift between the two generated phase-locked XUV fields, termed $\Delta\phi_{XUV}$. Figure 2(b) illustrates such shifts in the interferometry signal obtained at different NIR peak intensities. Generally, the minima and maxima shift toward lower energies as the NIR peak intensity increases. The collective shift of the spectral interference fringes, associated with $\Delta\phi_{XUV}$, as a function of the NIR intensity is summarized in Fig. 3(a). It is apparent that at moderate NIR peak intensities of up to ~25 TW cm^{-2}, the location of the minima and maxima in the interference pattern remains almost constant, while at peak intensities above 30 TW cm^{-2}, a redshift of the fringe pattern becomes similarly visible in the interferograms of all observed harmonics. In addition to the fringes moving toward lower photon energy as the intensity increases, the energy of the harmonics moves up. We emphasize that this blueshift of the individual harmonics does not affect the determination of $\Delta\phi_{XUV}$.

To quantify the high-harmonic phase shift, we employed the Takeda algorithm [48]. This algorithm extracts the spectral phase from the measured fringe patterns by filtering out the AC component in the Fourier domain (for details, see SI). We compared all retrieved phases to those obtained in the initial measurement conducted at the lowest NIR intensity. Consequently, the initial measurement serves as our phase reference ($\Delta\phi_{XUV} = 0$), and subsequent measurements reveal the relative phase shift compared to this baseline. It is important to note that this reference is arbitrary since the absolute phase is unknown; our interest lies solely in the relative phase—namely, how the phase $\Delta\phi_{XUV}$ changes with varying intensity levels. To quantify the phase shift $\Delta\phi_{XUV}$ for a given harmonic order, we calculated a weighted average of the phase shift across the measured intensity distribution of an individual harmonic order. This approach involves using the measured intensity

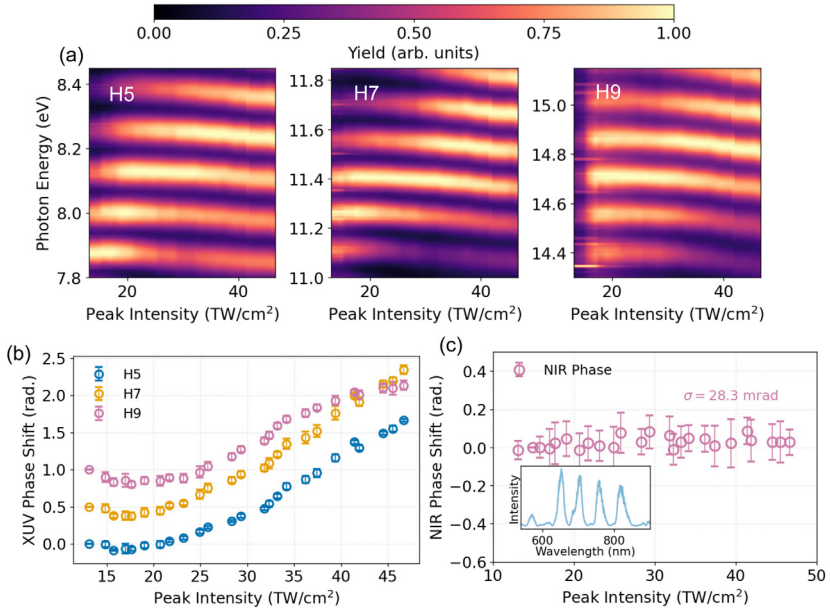

Fig. 3. Extraction of the $\overline{\Delta\phi}_{XUV}$ and $\overline{\Delta\phi}_{NIR}$ in SiO_2. (a) 2D maps of the intensity dependence of the spectral interferometry signal of the observed high harmonics. (b) Extracted XUV phase shift as a function of the NIR peak intensity (phases of H7 and H9 are offset vertically by 0.5 rad and 1 rad for visibility). To avoid visual clutter, we omit error bars on the intensity axis, which would arise from uncertainties due to beam profile and power fluctuations. (c) NIR spectral interferometry in SiO_2. The pink circles illustrate the intensity dependence of the NIR phase shift $\overline{\Delta\phi}_{NIR}$. The blue line in the inset shows the NIR-interference pattern. In the inset of panel (c), the vertical axis shows the normalized spectral intensity in arbitrary units. σ denotes the standard deviation of the extracted NIR phase shift, as determined from the fringe analysis.

profile of each harmonic as a weighting factor, ensuring that any small phase shifts within a harmonic peak are incorporated into the overall variance of the mean phase shift value. The weighted mean phase shift, $\overline{\Delta\phi}_{\mathrm{XUV}}$ of an individual harmonic order, can be expressed as

$$\overline{\Delta\phi}_{\mathrm{XUV}} = \frac{\sum_{i=1}^{N} Y_i \Delta\phi_i}{\sum_{i=1}^{N} Y_i}, \tag{1}$$

where Y_i represents the measured harmonic signal yield, and ϕ_i is the measured phase of the associated ith interference fringe maximum. The result of this analysis is shown in Fig. 3(b), where the resulting phase shift is visualized as a function of the NIR peak intensity for the three observed harmonics. After an almost flat region (with the exception of a small minimum around 17 TW cm^{-2}) up to ~22 TW cm^{-2}, the extracted phase for all harmonics substantially increases by more than 1 rad before reaching its maximum value at the highest experimentally accessible (i.e., nondestructive) intensity. Unlike H5 and H7, the extracted phase of H9 shows a saturation behavior at the highest NIR intensities.

In interpreting the observed $\overline{\Delta\phi}_{\mathrm{XUV}}$, it is ambiguous whether the phase alteration arises from the XUV-generation process (i.e., HHG) or if it stems from a phase accumulation of the time-delayed, fundamental NIR pulse $E_2(\omega, t-\tau)$ propagating through a region within the sample potentially modified by $E_1(\omega, t)$. The interaction of $E_1(\omega, t)$ with the sample may induce modifications in the optical properties via the generation of an electron–hole plasma, leading to an enhanced phase accumulation $\Delta\phi_{\mathrm{NIR}}$ of the time-delayed second NIR pulse [38]. Consequently, the resulting XUV phase would follow from the differential NIR phase via $\Delta\phi_{\mathrm{XUV}} = \mathcal{N}\Delta\phi_{\mathrm{NIR}}$, where $\mathcal{N}$ denotes the harmonic order. To investigate the potential imprint of the NIR phase on the XUV phase, spectral interferometry measurements were conducted in the NIR spectral range. The measurements were conducted under the same conditions as the XUV interferometry experiments, utilizing identical samples and maintaining an identical beam path up to the detection stage (see Fig. 1). Analogous to the procedure described for the XUV spectra, we used the Takeda algorithm to extract the intensity-dependent phase variation $\overline{\Delta\phi}_{\mathrm{NIR}}$ [purple circles in Fig. 3(c)]. The observed NIR phase shows no significant intensity dependence with a standard deviation of only 28.3 mrad indicating that the observed change of $\Delta\phi_{\mathrm{XUV}}$ is not due to propagation effects and is not inherited from the NIR phase. The absence of a detectable electron–hole plasma signature in the NIR interferometry measurements can be attributed to the small differential carrier density induced by the two excitation pulses, which is insufficient to cause a measurable change in the NIR phase (a detailed explanation and numerical estimate are provided in Supplement 1).

The same measurements as above were performed for monocrystalline MgO samples. The results are summarized in Fig. 4. As shown in Fig. 4(a), the overall shift of the interferometric pattern points in the opposite direction. At high intensities above ~ 15 TW cm^{-2}, a substantial shift of the interference pattern toward higher energies (blueshift) was observed. This behavior is further illustrated in Fig. 4(b), where the extracted $\overline{\Delta\phi}_{\mathrm{XUV}}$ as a function of NIR peak intensity is shown for the observed harmonics. The NIR spectral interferometry results shown in Fig. 4(c) again only display slight variations in the weighted mean NIR phase. Orientation-dependent measurements (see Supplement 1) reveal an anisotropic phase shift, consistent with earlier reports of polarization-sensitive excitation and HHG efficiency in MgO [31].

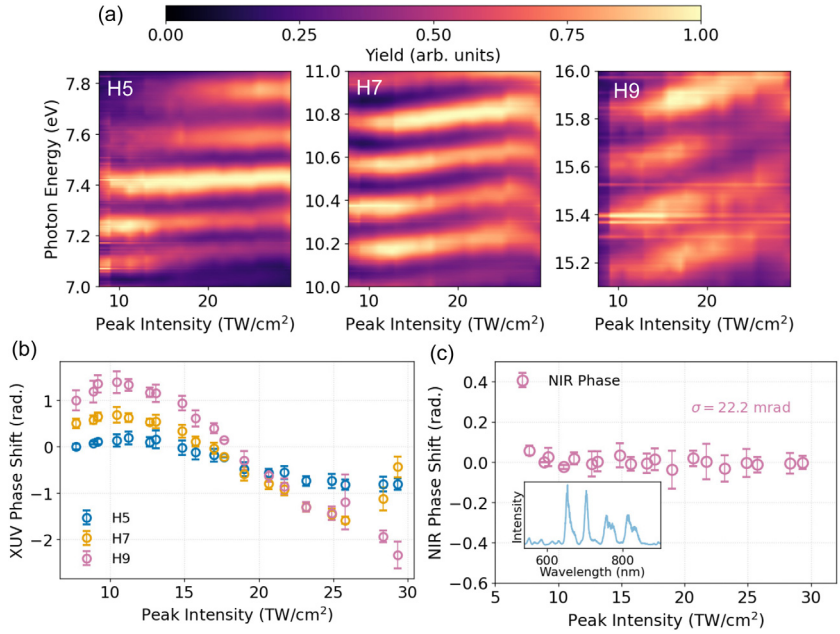

Fig. 4. Extraction of the $\overline{\Delta\phi}_{\mathrm{XUV}}$ and $\overline{\Delta\phi}_{\mathrm{NIR}}$ in MgO. (a) 2D maps of the intensity dependence of the spectral interferometry signal of the observed high harmonics. (b) Extracted XUV phase shift as a function of the NIR peak intensity (phases of H7 and H9 are offset vertically by 0.5 rad and 1 rad for visibility). To avoid visual clutter, we omit error bars on the intensity axis, which would arise from uncertainties due to beam profile and power fluctuations. (c) NIR spectral interferometry in MgO. The pink circles illustrate the intensity dependence of the NIR phase shift $\overline{\Delta\phi}_{\mathrm{NIR}}$. The blue line in the inset shows the NIR-interference pattern. In the inset of panel (c), the vertical axis shows the normalized spectral intensity in arbitrary units. σ denotes the standard deviation of the extracted NIR phase shift, as determined from the fringe analysis.

Additional measurements performed at various delays (also shown in Supplement 1) reveal a strong suppression of the high-harmonic phase variation with increasing NIR–NIR delay in the case of SiO_2 while the effect remains constant across the tested delays of 30, 40, and 50 fs in MgO. This can be attributed to the differing electron–hole recombination times and suggests that the observed intensity-dependent high-harmonic phase shifts are related to the photoexcited carrier densities.

Additional experimental observables extracted from the XUV interferometry measurements are summarized in Fig. 5. Panels (a) and (b) illustrate the central energy shifts of the observed harmonics in SiO_2 and MgO, respectively, both exhibiting continuous blueshifts. Notably, the energy shifts in MgO are significantly larger, reaching up to 0.6 eV, compared to a maximum of 0.3 eV in SiO_2. Figures 5(c) and 5(d) show the normalized fringe contrast of the interference patterns observed in SiO_2 and MgO as a function of the NIR peak intensity. To quantify the contrast of the spectral fringes, we have computed an average normalized fringe ratio for each harmonic order defined as

$$r = \frac{I_{\text{peak}} - 0.5 \times (I_{\text{valley,left}} + I_{\text{valley,right}})}{I_{\text{peak}} + 0.5 \times (I_{\text{valley,left}} + I_{\text{valley,right}})}, \tag{2}$$

where I_{peak} is the intensity at a fringe maximum, and $I_{\text{valley,left}}$ and $I_{\text{valley,right}}$ refer to the intensities of the neighboring minima.

While SiO_2 shows no characteristic trend across the full range of applied NIR intensities, MgO exhibits a clear reduction in fringe contrast with increasing intensity across all observed harmonic orders.

4. MODELING AND DISCUSSION

A. Modeling of XUV High-Harmonic Interferometry in Solids

To support our experimental findings, we performed analytical calculations and numerical simulations using a versatile set of models and tools. First, we computed the influence of an excited carrier population on the band structure of crystalline MgO using first-principle density-functional theory (DFT, details can be found in the SI). The comparison of ab initio calculations of the electronic distribution in pristine and strongly perturbed MgO reveals that due to state-blocking, the energy gap between the highest-lying valence band state and the lowest-lying conduction band state increases steadily as a function of the carrier concentration [see Figs. 6(a) and 6(b)]. At a carrier concentration of 1×10^{23} cm^{-3}, a bandgap widening of above 140 meV is predicted by our DFT calculations.

To model the spectral interferometry of HHG from solids, we numerically solved the SBEs in a two-band tight-binding approximation for cubic MgO along the Γ-X direction (for further details see SI) employing a phase-locked NIR pulse pair. Since excitation-induced variations in the electronic structure are not directly accounted for by the SBEs and are themselves extremely challenging to compute (see, e.g., Refs. [36,37]), we instead monitor the resulting high-harmonic interference pattern as a function of the bandgap E_g. This assumes that the conduction band population excited by the first strong NIR field dynamically modifies the bandgap, altering the HHG process induced by the second NIR field and leading to a variation in the high-harmonic phase.

For the simulations, we performed separate computations of single-pulse HHG for MgO with a bandgap varying from 7.5 to 8.0 eV in 10 meV steps. We subsequently compute the spectral interference of the emission with original bandgap at 7.5 eV and the time-delayed emission with varied bandgap. In this approach, the bandgap change is treated as a parameter, which allows us to study how bandgap changes manifest themselves as shifts of spectral interference fringes.

Figure 6(c) shows the bandgap dependence of the seventh harmonic interference pattern obtained from an SBE simulation at an NIR peak intensity of 30 TW cm^{-2} in MgO. A substantial frequency blueshift of the interference fringes for increasing bandgap (bandgap widening) is observed. The dashed gray lines in Fig. 6(c) emphasize this blueshift, revealing a linear increase in the fringe frequency of approximately 0.05. These results resemble the

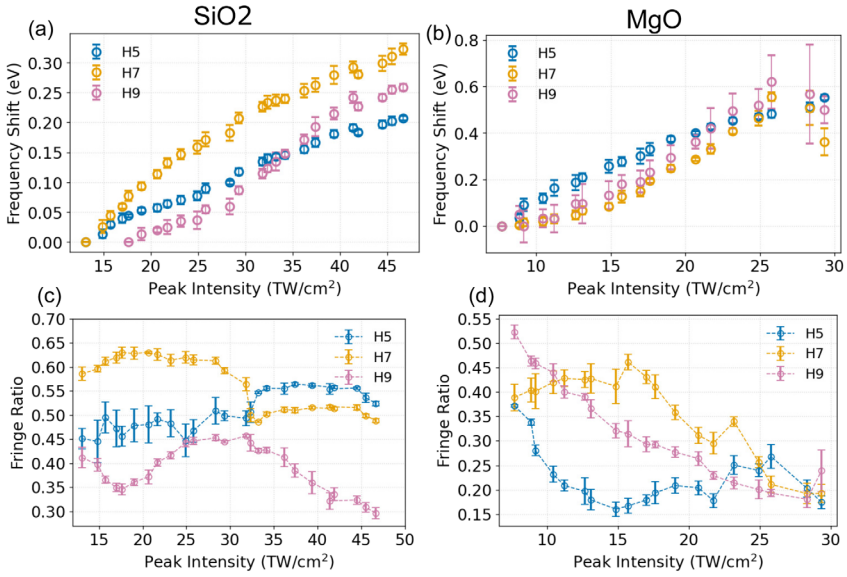

Fig. 5. Extraction of energy shifts and fringe ratios from the XUV interferometry measurements. (a) Energy shift of the individual harmonics as a function of excitation intensity in SiO_2. (b) Same as in (a) for MgO. (c) Extracted normalized fringe ratio of the observed odd harmonics according to Eq. (2) as a function of the NIR peak intensity in SiO_2. (d) Same as in (c) but for MgO.

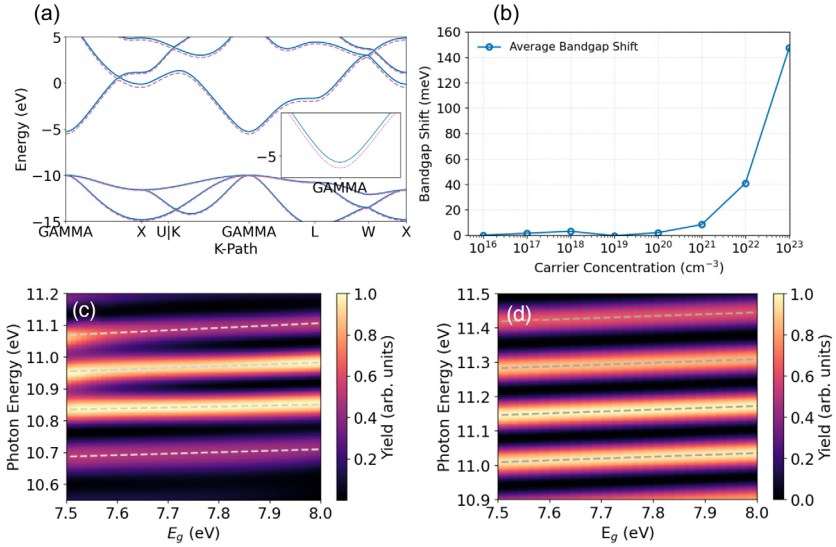

Fig. 6. Simulated bandgap renormalization and corresponding harmonic phase shifts. (a) Band structure of MgO obtained from DFT. The unperturbed system (purple lines) is compared to the excited system at a carrier concentration of 1×10^{23} cm^{-3} (blue lines), illustrating excitation-induced renormalization. (b) Averaged bandgap shift extracted from DFT calculations as a function of carrier density. (c) Shift of the seventh harmonic spectral interference pattern obtained from two-band SBE simulations with a fixed delay of 30 fs. (d) Same as (c), but using a semi-classical analytical model under the same excitation conditions.

experimental findings for MgO shown in Fig. 4(a), suggesting that the observed $\overline{\Delta\phi}_{\mathrm{XUV}}$ may be caused by a bandgap widening in the MgO crystals.

To analytically link high-harmonic phase shifts and bandgap modifications, we have employed an additional analytical, semi-classical two-band model for the calculation of HHG in solids as introduced in [49]. This model was numerically verified in [49] by comparing its predicted phase shifts to the phase shifts obtained from numerical solutions of the two-band semiconductor Bloch equations in length gauge. In brief, in the analytical model, we calculated classical trajectories within a two-band system under the assumption of low carrier inversion. Excitation is restricted to the Γ-point, to ensure unambiguous separation of long and short trajectories which are not found using the SBEs, as these allow for excitation along the entire band structure [50] according to the k-dependent transition dipole moment and band energy separation.

Electron and hole ($\lambda \in \{e, h\}$) wavepacket trajectories $x^{\lambda}(t)$ for different excitation times t_i are determined by classical integration of the group velocity $v^{\lambda}_{g(k(t))}$ over time, where k denotes the crystal momentum:

$$x^{\lambda}(t) = \int_{t_i}^{t} v_g^{\lambda}(k(\tau))\mathrm{d}\tau. \tag{3}$$

Recombination is assumed to occur when the spatial displacement between the electron and hole becomes zero:

$$\Delta x(t_r) = x^{e}(t_r) - x^{h}(t_r) = 0. \tag{4}$$

Here, t_r represents the recombination time. The photon energy emitted by a given trajectory corresponds to the energy difference $\Delta\varepsilon$ between the carriers at the moment of recombination. To assess the influence of bandgap variations on the phase of the associated interband current, we calculated the phase of the emitted light using the semi-classical action:

$$S(t_r) = \int_{t_i}^{t_r} \Delta\varepsilon(k(\tau))\mathrm{d}\tau. \tag{5}$$

From $S(t_r)$, we can evaluate the dipole phase [51] via

$$\phi = \mathcal{N}\left(\omega_0 t_r + \frac{\pi}{2}\right) - S(t_r), \tag{6}$$

with $\mathcal{N}$ being the harmonic order of the fundamental frequency ω_0. Under the assumption of small bandgap variations, the resulting phase difference can be approximated by

$$\Delta\phi \approx -\Delta E_g \Delta t \quad \text{with} \quad \Delta t = t_r - t_i. \tag{7}$$

For MgO, we obtained a characteristic excursion time of $\Delta t \sim 1.5$ fs for the seventh harmonic order in [49], which was obtained by fitting the phase shifts from the two-band SBEs [Fig. 6(c)] with Eq. (7). Results for the relationship between the frequency shift of the interference spectrum and the bandgap variation for the seventh harmonic obtained from the analytical model are presented in Fig. 6(d). A linear relationship between the shift of the interference pattern and the bandgap variation ΔE_g with an average slope of ~ 0.05 (indicated by the gray dashed lines, identical to the slope observed in the SBE results) can be observed. Again, the qualitative agreement with the experimental results shown in Fig. 4 indicates that indeed photo-induced bandgap dynamics and associated variations of the dipole phase can be held responsible for the experimentally observed $\overline{\Delta\phi}_{\mathrm{XUV}}$.

B. Discussion and Interpretation of the Results

Since the photon energies of all observed high-order harmonics lie above the bandgap, with the exception of H5, which lies close to the bandgap of both SiO_2 and MgO (~7.8 eV) and may partially overlap with it, we expect interband recollisions to provide the dominant contribution to the harmonic radiation.

This is also corroborated by our SBE results and is in agreement with recent studies concluding that above-bandgap harmonics

are dominated by the interband recollision mechanism [52,53]. Moreover, since the photon energies of the observed harmonics (H5–H9) range from approximately 8 eV to 14 eV, i.e., lie above or near the bandgaps of the investigated materials, a two-band description, considering only the valence and conduction bands, is adequate. This is justified by the fact that, in our simulations, the combined energy width of these two bands exceeds 8.6 eV (details in SI).

The phase variation of the XUV harmonics is interpreted as arising from a modification of the high-harmonic phase of the second XUV pulse. This modification results from the interaction of the first NIR pulse with the sample, which alters the optical properties of the material. This phase shift, observed at a delay well beyond the pulse duration, cannot arise from coherent field-driven effects such as the AC Stark shift or free induction decay, but instead points to an incoherent, longer-lived excitation of carriers that most plausibly induces a transient modification of the band structure, with bandgap renormalization expected to play the dominant role. The reasoning behind a positive or negative phase shift can be at least partially understood as follows: according to Eq. (7), the phase decreases if the bandgap increases [note the minus sign in Eq. (7)]. The phase can be viewed as the accumulated action of the electron following excitation, hence a change in energy directly affects the phase. While the time the electron spends during acceleration also changes with changing bandgap, we found the influence of this change to be negligible compared to the band energy changes in our simulations. In contrast, if the bandgap decreases, the opposite occurs and the phase increases.

Several recent studies have proposed that in strongly excited fused silica, the bandgap tends to shrink [36,37]. Although directly measuring the transient bandgap modulation is challenging, especially at intrapulse timescales [38], several indirect evidences have been obtained, indicating a significant shrinkage of the bandgap in photoexcited SiO_2 [41], up to several eV. Conversely, in crystalline materials, an opposite behavior has been reported [40]. Due to Pauli blocking of the available and allowed energy states close to the conduction band edge and ground-state bleaching (i.e., a significant reduction of the ground-state population), the effective energy required for an electron to be promoted from the valence to the conduction band increases. This state blocking, or bandgap widening, has been observed in many different crystalline materials [39] and is often connected to the Burstein–Moss effect [54]. One possible explanation for the observed differences between SiO_2 and MgO might lie in the lack of a well-defined band structure in amorphous SiO_2. In such materials, due to the existing crystalline short-range order, energy landscapes form in small clusters of the material. However, over a longer range or larger volume, the band structure washes out, resulting in a large number of available excited states. This inhibits the state blocking observed in crystalline materials, where only specific, well-defined energy levels are available for electron excitation. The microscopic mechanism leading to the bandgap narrowing in fused silica is still a topic of intense debate. Recent calculations suggest that strong-field-induced electronic charge redistribution may lead to a rearrangement of atoms, resulting in altered bonding strength and a corresponding decrease in the bandgap [36]. Additionally, intrinsic and photo-induced impurities and defects can modify the electronic landscape, thereby influencing the band structure and bandgap. Currently, no unified theory exists that simultaneously captures these effects alongside reliable modeling of photo-induced band structure variations, particularly for amorphous SiO_2. Consequently, calculations fully explaining the opposing trends observed for MgO and SiO_2 are beyond the scope of this work. However, our interpretation is strongly supported by previous experimental and theoretical studies.

As described above, the opposite signs of the phase variation can approximately be assigned to different signs of the bandgap variation due to the presence of an electron–hole plasma. In Figs. 7(a) and 7(b), we estimate the corresponding ΔE_g values from the measured $\overline{\Delta\phi}_{\mathrm{XUV}}$ using Eq. (7), under the assumption that the observed phase shift is primarily due to bandgap variations. This results in a maximum bandgap widening of ~ 1 eV in the case of MgO [see Fig. 7(b)] and a bandgap shrinkage of ~ 0.8 eV for SiO_2 [Fig. 7(a)] using characteristic excursion times of $\Delta t \sim 1.5$ fs as determined earlier. Figure 7 contains error bars reflecting the NIR phase uncertainty, propagated as $2\sigma\mathcal{N}$, to account for harmonic-order dependent scaling. These estimated bandgap variations are consistent with trends observed in previous studies [41] and numerical simulations of strong-field-induced bandgap shifts in wide-bandgap materials and indicate the possibility of tracking bandgap dynamics with sub-fs temporal precision using XUV spectral interferometry in wide-bandgap solids.

We emphasize that Eq. (7) is a simplified model based on specific assumptions. Nevertheless, the consistency between experiment and simulation provides compelling support for our hypothesis-driven interpretation, and we find the bandgap extraction highly insightful, as it underscores the broad applicability of our experimental technique for determining a key material property, which is of significant interest both for fundamental research and potential technological applications.

Finally, the extracted frequency shifts and fringe ratios of the individual harmonics can be analyzed and interpreted in terms of

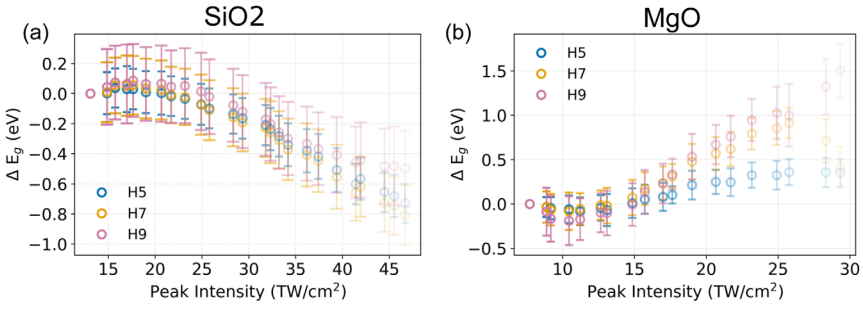

Fig. 7. (a) Extracted bandgap variation as a function of the NIR peak intensity in SiO_2 obtained with the help of Eq. (7). (b) Same as in (a) but for MgO. Results in the high-intensity regime are faded due to the limited validity of Eq. (7) in this regime and the underlying approximations. Error bars calculated as $2\sigma\mathcal{N}$, where σ is the standard deviation of the NIR phase noise, and $\mathcal{N}$ is the harmonic order.

the generated conduction band electron densities. Assuming that the frequency shifts of the harmonics are linked to an excitation-induced blueshift, a considerably higher density of photoexcited electron–hole pairs, despite a very similar bandgap, was generated in MgO. This blueshift arises from plasma-induced refractive index changes and occurs irrespective of the direction of the high-harmonic phase shift, confirming that it is governed by carrier density rather than bandgap dynamics. Additionally, the lifetime of the electron–hole plasma in MgO was reported as being significantly longer ($\tau_L \approx$, 1.5 ps [55]) compared to SiO_2 ($\tau_L \approx$, 150 fs [56]). Further evidence for higher plasma densities in MgO arises from the fringe contrast in the interferometric measurements [see Fig. 5(c) for SiO_2 and (d) for MgO]. As shown in Ref. [49], a faster dephasing, characterized by a decrease of the dephasing time T_2, leads to a suppression of the HHG yield, which can be approximately described by

$$Y \propto e^{-\frac{\tau}{T_2}} T_2 \left(1 - e^{-\frac{\tau}{T_2}}\right), \tag{8}$$

with τ being the time delay.

A carrier population generated by the leading pulse will enhance the electron–electron scattering rate and thus the dephasing during the HHG induced by the trailing pulse due to the presence of the electron–hole pairs as has been measured in photon-echo experiments in the single-photon weak-field limit [57]. The increased dephasing suppresses the harmonic yield generated by the trailing pulse [58], leading to a weaker contribution from the second interference source and, consequently, an intensity-dependent decrease in fringe contrast as experimentally observed in Figs. 5(c) and 5(d), compared to a perfect intensity modulation in the interferogram of two equal HHG emissions. Based on earlier two-band SBE simulations [49], we note that while reduced dephasing times can lead to minor phase shifts in the high-harmonic emission, these effects are accompanied by a strong suppression of the HHG yield, making it unlikely that the observed phase shifts in our experiment originate from dephasing.

5. CONCLUSION

In conclusion, we have expanded high-harmonic spectroscopy of solid-state systems to XUV spectral interferometry, a technique previously limited to gas-phase and molecular systems. We analyzed the intensity-dependent variation of the high-harmonic phase using XUV spectral interferometry and interpret these results in terms of transient alterations of the electronic structure. We observed fundamentally different behavior in the two materials studied, amorphous SiO_2 and crystalline MgO, which we attribute to differences in their photo-induced bandgap dynamics and dipole phase response. While these observations may be indicative of trends associated with amorphous and crystalline order, further studies on a broader range of materials will be necessary to confirm whether such distinctions hold generally.

Our results highlight the versatility of high-harmonic spectroscopy for investigating ultrafast carrier dynamics and their resulting effects in solids. We also demonstrate the potential of XUV interferometry as an all-optical technique for probing band structure dynamics with the potential for subcycle accuracy. The presented strategy is not limited to the specific classes of materials studied here but represents a widely applicable experimental technique with potential applications in ultrafast metrology of semiconductors, thin films, and two-dimensional materials. Furthermore, high-harmonic interferometry may enable the decoding of various ultrafast electronic and structural dynamics when performed in different wavelength and delay ranges. Notably, the interferometric approach could also provide a viable strategy for all-optical probing of electron–hole coherence times, thereby offering direct access to the dephasing time of photoexcited electron–hole pairs.

Funding. European Research Council (101041819); Nederlandse Organisatie voor Wetenschappelijk Onderzoek (VI.Vidi.223.133); Deutsche Forschungsgemeinschaft (533828881, 441234705).

Acknowledgment. Part of this work was conducted at the Advanced Research Center for Nanolithography, a public–private partnership between the University of Amsterdam (UvA), Vrije Universiteit Amsterdam (VU), Rijksuniversiteit Groningen (RUG), The Netherlands Organization for Scientific Research (NWO), and the semiconductor equipment manufacturer ASML and was (partly) financed by "Toeslag voor Topconsortia voor Kennis en Innovatie (TKI)" from the Dutch Ministry of Economic Affairs and Climate Policy.

Disclosures. The authors declare no conflicts of interest.

Data availability. Data underlying the results presented in this paper are not publicly available at this time but may be obtained from the authors upon reasonable request.

Supplemental document. See Supplement 1 for supporting content.

REFERENCES

1. C. Iaconis and I. A. Walmsley, "Self-referencing spectral interferometry for measuring ultrashort optical pulses," IEEE J. Quantum Electron. **35**, 501–509 (1999).
2. C. Froehly, A. Lacourt, and J. C. Viénot, "Time impulse response and time frequency response of optical pupils: experimental confirmations and applications," Nouv. Rev. d'Optique **4**, 183 (1973).
3. L. Lepetit, G. Chériaux, and M. Joffre, "Linear techniques of phase measurement by femtosecond spectral interferometry for applications in spectroscopy," J. Opt. Soc. Am. B **12**, 2467–2474 (1995).
4. A. L'Huillier and P. Balcou, "High-order harmonic generation in rare gases with a 1-ps 1053-nm laser," Phys. Rev. Lett. **70**, 774 (1993).
5. P.-M. Paul, E. S. Toma, P. Breger, *et al.*, "Observation of a train of attosecond pulses from high harmonic generation," Science **292**, 1689–1692 (2001).
6. M. Hentschel, R. Kienberger, C. Spielmann, *et al.*, "Attosecond metrology," Nature **414**, 509–513 (2001).
7. A. L'Huillier, "Nobel lecture: the route to attosecond pulses," Rev. Mod. Phys. **96**, 030503 (2024).
8. F. Krausz, "Nobel lecture: sub-atomic motions," Rev. Mod. Phys. **96**, 030502 (2024).
9. P. Agostini, "Nobel lecture: genesis and applications of attosecond pulse trains," Rev. Mod. Phys. **96**, 030501 (2024).
10. P. B. Corkum and F. Krausz, "Attosecond science," Nat. Phys. **3**, 381–387 (2007).
11. P. Tzallas, D. Charalambidis, N. Papadogiannis, *et al.*, "Direct observation of attosecond light bunching," Nature **426**, 267–271 (2003).
12. D. Azoury, O. Kneller, S. Rozen, *et al.*, "Electronic wavefunctions probed by all-optical attosecond interferometry," Nat. Photonics **13**, 54–59 (2019).
13. O. Kneller, D. Azoury, Y. Federman, *et al.*, "A look under the tunnelling barrier via attosecond-gated interferometry," Nat. Photonics **16**, 304–310 (2022).
14. A. H. Chin, O. G. Calderón, and J. Kono, "Extreme midinfrared nonlinear optics in semiconductors," Phys. Rev. Lett. **86**, 3292 (2001).
15. S. Ghimire, A. D. DiChiara, E. Sistrunk, *et al.*, "Observation of high-order harmonic generation in a bulk crystal," Nat. Phys. **7**, 138–141 (2011).
16. Z. Nie, L. Guery, E. Molinero, *et al.*, "Following the nonthermal phase transition in niobium dioxide by time-resolved harmonic spectroscopy," Phys. Rev. Lett. **131**, 243201 (2023).
17. M. L. van der Geest, J. J. de Boer, K. Murzyn, *et al.*, "Transient high-harmonic spectroscopy in an inorganic–organic lead halide perovskite," J. Phys. Chem. Lett. **14**, 10810–10818 (2023).

18. A. Lanin, E. Stepanov, A. Fedotov, *et al.*, "Mapping the electron band structure by intraband high-harmonic generation in solids," Optica **4**, 516–519 (2017).
19. T. T. Luu, M. Garg, S. Y. Kruchinin, *et al.*, "Extreme ultraviolet high-harmonic spectroscopy of solids," Nature **521**, 498–502 (2015).
20. O. Schubert, M. Hohenleutner, F. Langer, *et al.*, "Sub-cycle control of terahertz high-harmonic generation by dynamical Bloch oscillations," Nat. Photonics **8**, 119–123 (2014).
21. B. Zaks, R.-B. Liu, and M. S. Sherwin, "Experimental observation of electron–hole recollisions," Nature **483**, 580–583 (2012).
22. J. Lu, E. F. Cunningham, Y. S. You, *et al.*, "Interferometry of dipole phase in high harmonics from solids," Nat. Photonics **13**, 96–100 (2019).
23. P. B. Corkum, "Plasma perspective on strong field multiphoton ionization," Phys. Rev. Lett. **71**, 1994 (1993).
24. M. Lewenstein, P. Balcou, M. Y. Ivanov, *et al.*, "Theory of high-harmonic generation by low-frequency laser fields," Phys. Rev. A **49**, 2117 (1994).
25. M. Lewenstein, P. Salieres, and A. L'Huillier, "Phase of the atomic polarization in high-order harmonic generation," Phys. Rev. A **52**, 4747 (1995).
26. K. Uchida and K. Tanaka, "High harmonic Mach–Zehnder interferometer for probing sub-laser-cycle electron dynamics in solids," Opt. **11**, 1130–1137 (2024).
27. P. Jürgens, B. Liewehr, B. Kruse, *et al.*, "Origin of strong-field-induced low-order harmonic generation in amorphous quartz," Nat. Phys. **16**, 1035–1039 (2020).
28. Y. S. You, Y. Yin, Y. Wu, *et al.*, "High-harmonic generation in amorphous solids," Nat Commun **8**, 724 (2017).
29. S. D. Roscam Abbing, R. Kolkowski, Z.-Y. Zhang, *et al.*, "Extreme-ultraviolet shaping and imaging by high-harmonic generation from nanostructured silica," Phys. Rev. Lett. **128**, 223902 (2022).
30. Y. S. You, D. A. Reis, and S. Ghimire, "Anisotropic high-harmonic generation in bulk crystals," Nat. Phys. **13**, 345–349 (2017).
31. P. Jürgens, S. D. Roscam Abbing, M. Mero, *et al.*, "Linking high-harmonic generation and strong-field ionization in bulk crystals," ACS Photonics **11**, 247–256 (2024).
32. H. Hübener, M. A. Sentef, U. De Giovannini, *et al.*, "Creating stable floquet–weyl semimetals by laser-driving of 3d dirac materials," Nat. Commun. **8**, 13940 (2017).
33. A. J. Uzan-Narovlansky, Á. Jiménez-Galán, G. Orenstein, *et al.*, "Observation of light-driven band structure via multiband high-harmonic spectroscopy," Nat. Photonics **16**, 428–432 (2022).
34. A.-P. Jauho and K. Johnsen, "Dynamical Franz-Keldysh effect," Phys. Rev. Lett. **76**, 4576 (1996).
35. M. Lucchini, S. A. Sato, A. Ludwig, *et al.*, "Attosecond dynamical Franz-Keldysh effect in polycrystalline diamond," Science **353**, 916–919 (2016).
36. A. Tsaturyan, E. Kachan, R. Stoian, *et al.*, "Ultrafast bandgap narrowing and cohesion loss of photoexcited fused silica," J. Chem. Phys. **156**, 224301 (2022).
37. A. A. Tsaturyan, E. Kachan, R. Stoian, *et al.*, "Excited-state dynamics and optical properties of silica under ultrafast laser irradiation," Adv. Phys. Res **4**, 2400106 (2024).
38. P. Jürgens, C. L. Garcia, P. Balling, *et al.*, "Diagnostics of fs laser-induced plasmas in solid dielectrics," Laser Photonics Rev. **18**, 2301114 (2024).
39. K. Saw, N. Aznan, F. Yam, *et al.*, "New insights on the burstein-moss shift and band gap narrowing in indium-doped zinc oxide thin films," PloS one **10**, e0141180 (2015).
40. M. Feneberg, S. Osterburg, K. Lange, *et al.*, "Band gap renormalization and Burstein-Moss effect in silicon-and germanium-doped wurtzite GaN up to 10 20 cm- 3," Phys. Rev. B **90**, 075203 (2014).
41. T. Winkler, P. Balling, B. Zielinski, *et al.*, "Unveiling nonlinear regimes of light amplification in fused silica with femtosecond imaging spectroscopy," Phys. Rev. Res **2**, 023341 (2020).
42. D. Golde, T. Meier, and S. W. Koch, "Microscopic analysis of extreme nonlinear optics in semiconductor nanostructures," J. Opt. Soc. Am. B **23**, 2559–2565 (2006).
43. H. Haug and S. W. Koch, *Quantum Theory of the Optical and Electronic Properties of Semiconductors* (World Scientific Publishing Company, 2009).
44. T. Witting, F. Frank, C. A. Arrell, *et al.*, "Characterization of high-intensity sub-4-fs laser pulses using spatially encoded spectral shearing interferometry," Opt. Lett. **36**, 1680–1682 (2011).
45. L.-M. Koll, L. Maikowski, L. Drescher, *et al.*, "Phase-locking of time-delayed attosecond XUV pulse pairs," Opt Express **30**, 7082–7095 (2022).
46. H. Allegre, J. J. Broughton, T. Klee, *et al.*, "Extension of high-harmonic generation cutoff in solids to 50 eV using MgO," Opt. Lett. **50**, 1492–1495 (2025).
47. Z. Chang, A. Rundquist, H. Wang, *et al.*, "Temporal phase control of soft-x-ray harmonic emission," Phys. Rev. A **58**, R30 (1998).
48. M. Takeda, H. Ina, and S. Kobayashi, "Fourier-transform method of fringe-pattern analysis for computer-based topography and interferometry," J. Opt. Soc. Am. **72**, 156–160 (1982).
49. B. De Keijzer, P. J. van Essen, and P. M. Kraus, "Effect of photoexcitation on high-harmonic generation in semiconductors," J. Opt. Soc. Am. B **41**, 1754–1763 (2024).
50. U. Huttner, K. Schuh, J. V. Moloney, *et al.*, "Similarities and differences between high-harmonic generation in atoms and solids," J. Opt. Soc. Am. B **33**, C22–C29 (2016).
51. S. Carlström, J. Preclíková, E. Lorek, *et al.*, "Spatially and spectrally resolved quantum path interference with chirped driving pulses," New J. Phys. **18**, 123032 (2016).
52. G. Vampa, C. McDonald, G. Orlando, *et al.*, "Theoretical analysis of high-harmonic generation in solids," Phys. Rev. Lett. **113**, 073901 (2014).
53. L. Yue and M. B. Gaarde, "Imperfect recollisions in high-harmonic generation in solids," Phys. Rev. Lett. **124**, 153204 (2020).
54. E. Burstein, "Anomalous optical absorption limit in InSb," Phys. Rev. **93**, 632 (1954).
55. S. Guizard, P. Martin, P. Daguzan, *et al.*, "Contrasted behaviour of an electron gas in MgO, Al2O3 and SiO2," Europhys. Lett. **29**, 401 (1995).
56. P. Martin, S. Guizard, P. Daguzan, *et al.*, "Subpicosecond study of carrier trapping dynamics in wide-band-gap crystals," Phys. Rev. B **55**, 5799 (1997).
57. P. Becker, H. Fragnito, C. B. Cruz, *et al.*, "Femtosecond photon echoes from band-to-band transitions in gaas," Phys. Rev. Lett. **61**, 1647 (1988).
58. C. Heide, Y. Kobayashi, A. C. Johnson, *et al.*, "Probing electron-hole coherence in strongly driven 2D materials using high-harmonic generation," Optica **9**, 512–516 (2022).